Supplement of Ocean Sci., 20, 1067–1086, 2024
https://doi.org/10.5194/os-20-1067-2024-supplement

Ocean Science Open Access EGU

Supplement of

An assessment of equatorial Atlantic interannual variability in Ocean Model Intercomparison Project (OMIP) simulations

Arthur Prigent and Riccardo Farneti

Correspondence to: Arthur Prigent (aprigent@ictp.it)

The content of this file is:

- Supplementary Figures S1 to S14
- Supplementary Table S1
- Supplementary Texts S1 to S3

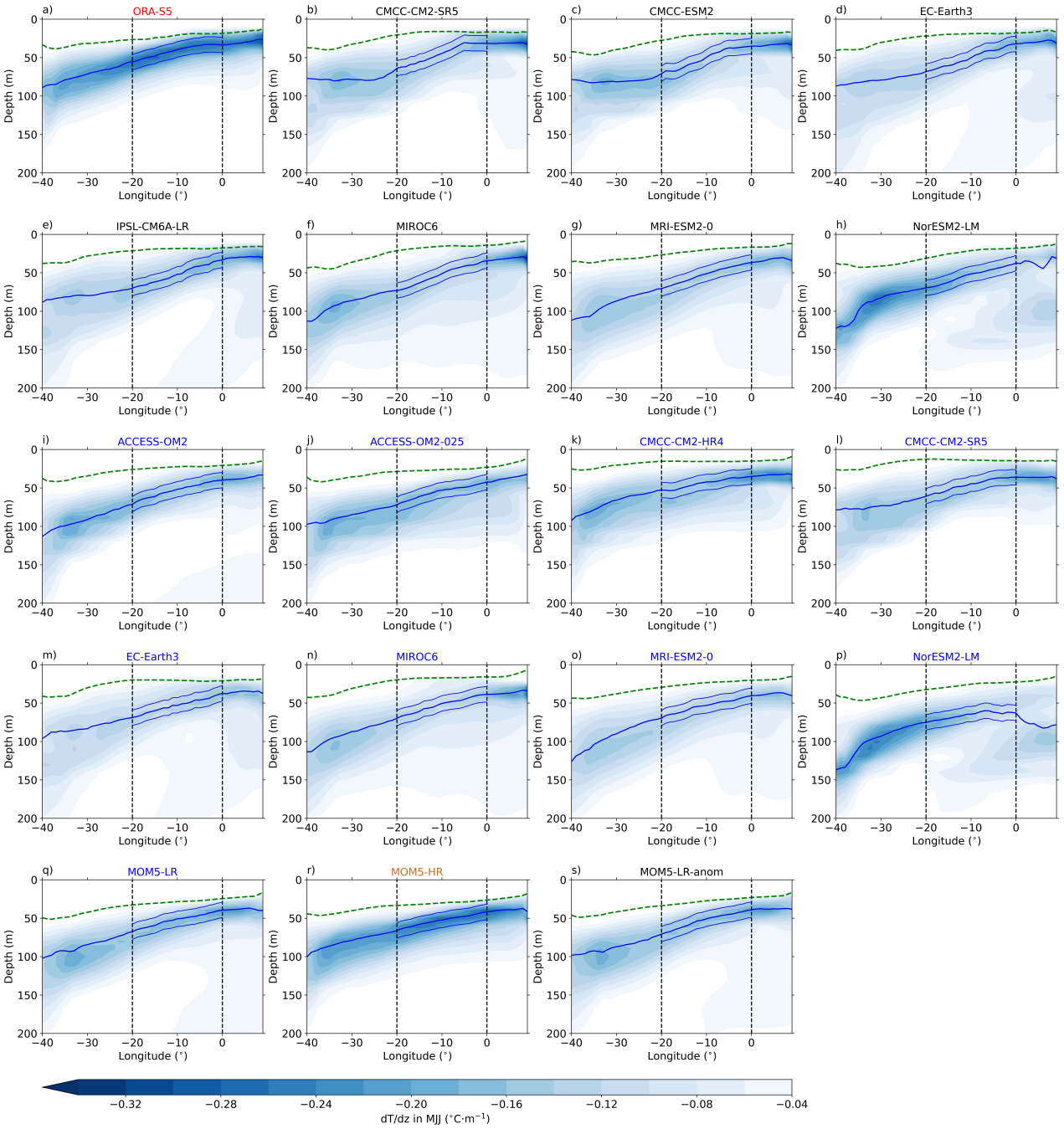

Figure S1. Upper 200 m equatorial Atlantic vertical temperature gradient in MJJ averaged between 3°S-3°N for (a) ORA-S5, (b-h) OMIP1 models, (i-p) OMIP2 models, and (q-s) the MOM5-LR, MOM5-HR, and MOM5-LR-anom experiments over the period from January 1985 to December 2004. The dashed green line represents the MLD in MJJ. The solid blue line is the depth of the maximum dT/dz in MJJ and the thin blue lines are located ± 10 m around the depth of the maximum dT/dz. Vertical dashed black lines depict the ATL3 region.

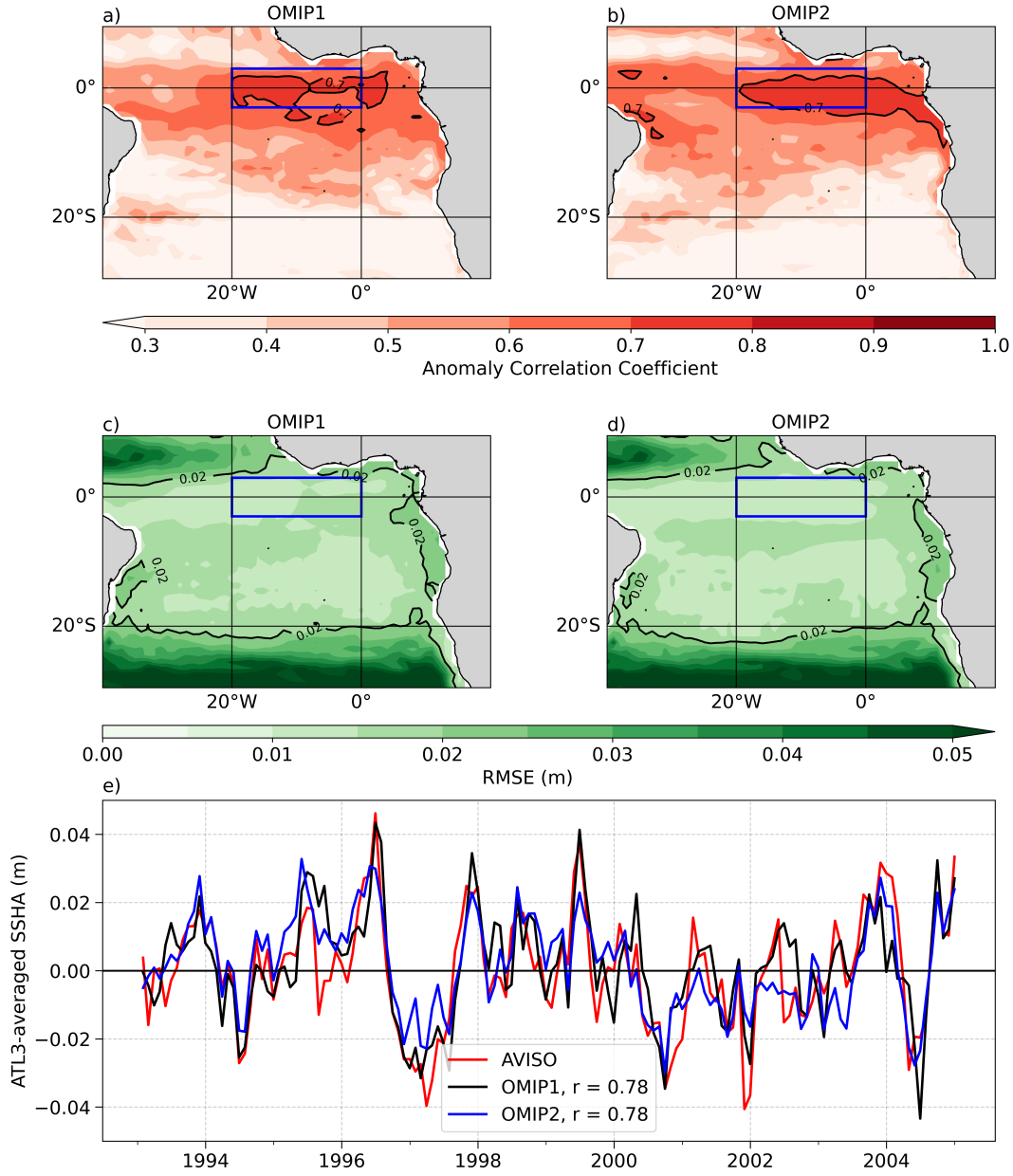

Figure S2. Anomaly correlation (a, b) and root-mean-square error (RMSE; c, d) of OMIP1 and OMIP2 simulations with AVISO over the period January 1993 to December 2004. (e) Timeseries depicting ATL3-averaged monthly SSH anomalies from January 1993 to December 2004 for the AVISO product (red), the OMIP1 ensemble mean (black) and for the OMIP2 ensemble mean (blue). The legend denotes Pearson correlations between the OMIP1 and OMIP2 ensemble means and the AVISO product. The blue box depicts the ATL3 region (20°W-0°E, 3°S-3°N).

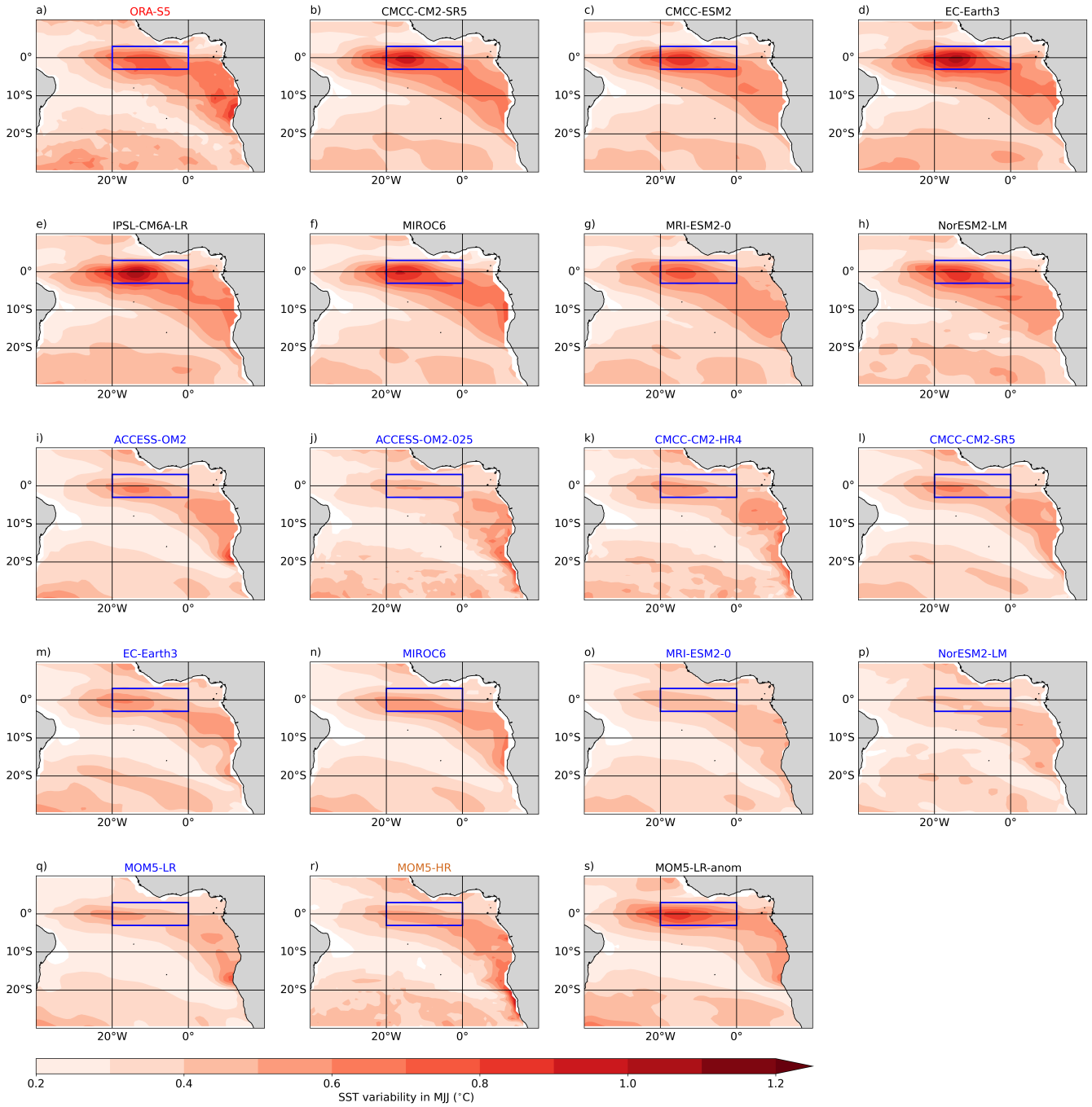

Figure S3. Tropical Atlantic interannual SST variability in MJJ. Standard deviation of the MJJ-averaged SST anomalies for (a) ORA-S5, (b-h) OMIP1 models, (i-p) OMIP2 models, and (q-s) the MOM5-LR, MOM5-HR, and MOM5-LR-anom experiments over the period from January 1985 to December 2004. The blue box depicts the ATL3 region (20°W-0°E, 3°S-3°N).

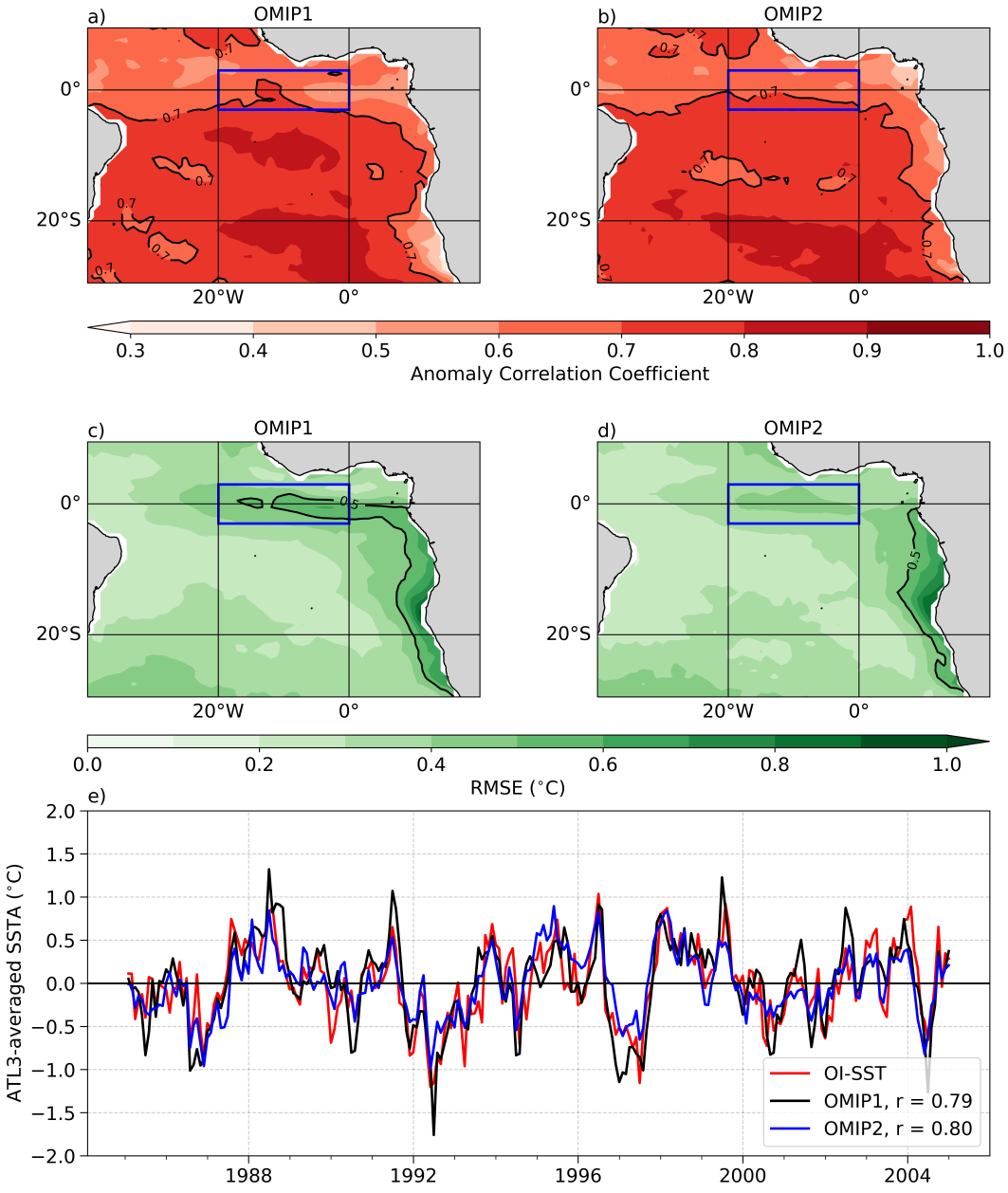

Figure S4. Anomaly correlation (a, b) and root-mean-square error (RMSE; c, d) of OMIP1 and OMIP2 simulations with OI-SST over the period January 1985 to December 2004. (e) Timeseries depicting ATL3-averaged monthly SST anomalies from January 1985 to December 2004 for the OI-SST (red), the OMIP1 ensemble mean (black) and for the OMIP2 ensemble mean (blue). The legend denotes Pearson correlations between the OMIP1 and OMIP2 ensemble means and the OI-SST. The blue box depicts the ATL3 region (20°W-0°E, 3°S-3°N).

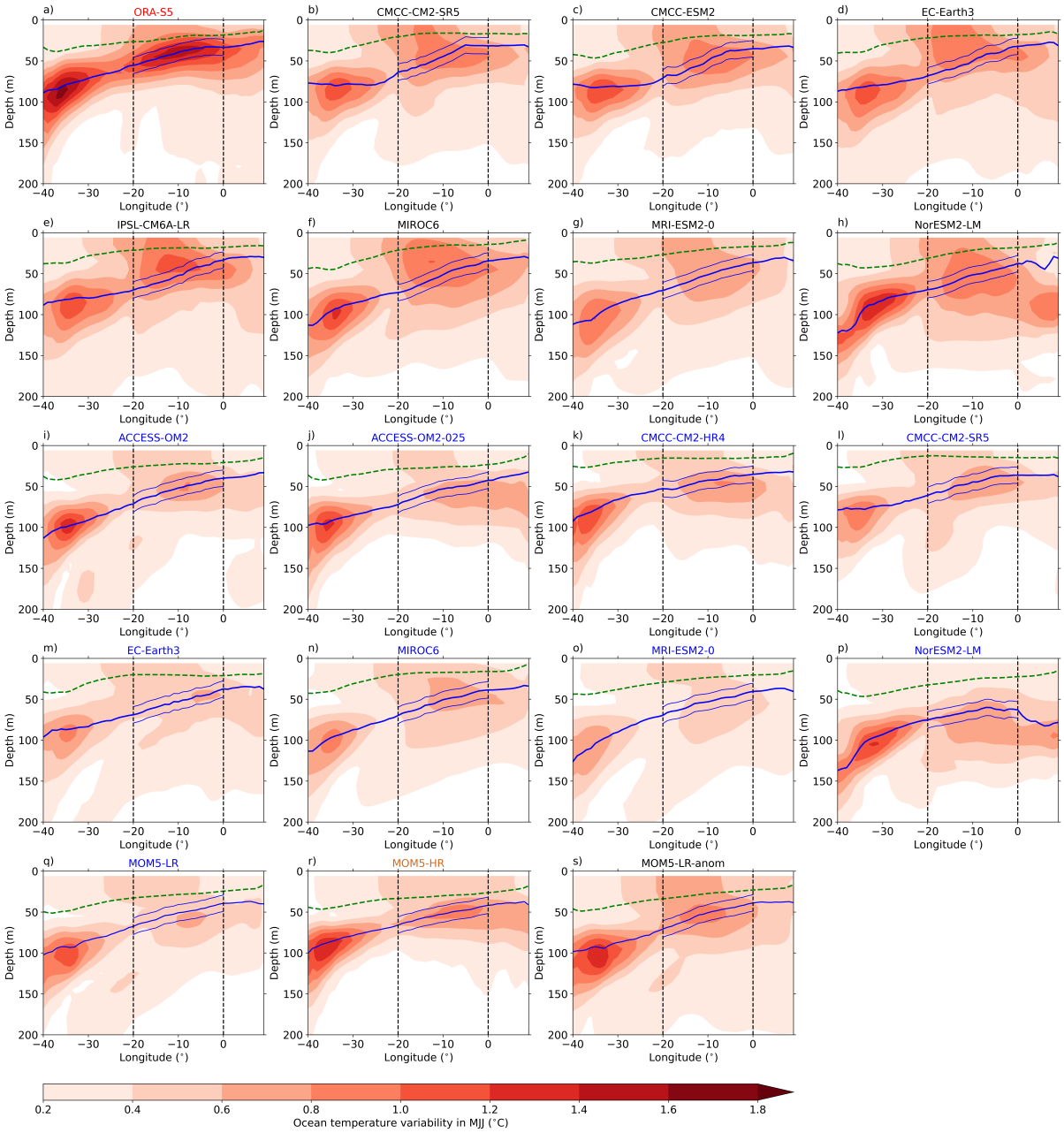

Figure S5. Upper 200 m equatorial Atlantic interannual temperature variability in MJJ. Standard deviation of the MJJ-averaged temperature anomalies averaged between 3°S-3°N for (a) ORA-S5, (b-h) OMIP1 models, (i-p) OMIP2 models, and (q-s) the MOM5-LR, MOM5-HR, and MOM5-LR-anom experiments over the period January 1985 to December 2004. The dashed green line represents the MLD in MJJ. The solid blue line is the depth of the maximum dT/dz in MJJ and the thin blue lines are located ± 10 m around the depth of the maximum dT/dz. Vertical dashed black lines depict the ATL3 region.

Supplementary Text S1: Evaluation of MOM5-LR, MOM5-HR and MOM5-LR-anom simulations

The tropical Atlantic SST and equatorial Atlantic Ocean temperature (40°W-10°E, 3°S-3°N) mean-states, monthly climatologies and interannual variability from MOM5-LR and MOM5-HR are compared to ORA-S5 over the period from January 1985 to December 2004 in Figures S6, S7, S8, and S9. Additionally, the sensitivity experiment MOM5-LR-anom is also compared to MOM5-LR.

The tropical Atlantic SST mean-state in ORA-S5, MOM5-LR and MOM5-HR is shown in Figures S6a, b, and c, respectively. Even though the SST pattern in MOM5-LR and MOM5-HR is very similar to ORA-S5, both simulations feature a warm SST bias in the eastern tropical Atlantic ocean (Figures S6d, e). The magnitude and pattern of these warm biases resemble the ones that can be found in the OMIP1 and OMIP2 ensemble means (Farneti et al., 2022). The warm ATL3-averaged SST bias in MOM5-LR and MOM5-HR relative to ORA-S5 is of 0.30 °C and 0.47 °C, respectively. On the contrary, the warm SST bias in the southeastern tropical Atlantic is larger in MOM5-LR (Figure S6d) than in MOM5-HR (Figure S6e). MOM5-LR-anom (Figure S6f) experiences a cooling of the SST in the EEA relative to MOM5-LR. In the southeastern tropical Atlantic south of 20°S, MOM5-LR-anom features a strong warming (>0.8 °C) relative to MOM5-LR.

Monthly climatologies of the ATL3-averaged SST (Figure S7a) show that both MOM5-LR and MOM5-HR simulations feature a warm SST bias in comparison to ORA-S5. The warm bias is more pronounced in MOM5-HR than in MOM5-LR. MOM5-LR-anom depicts warmer (colder) SSTs than MOM5-LR in January-February-March (July-August-September) (Figure S7a). Monthly climatologies of the standard deviation of the ATL3-averaged SST anomalies (Figure S7b) show that both MOM5-LR and MOM5-HR have too weak interannual SST variability in comparison to ORA-S5. The interannual SST variability in MOM5-HR is slightly stronger than in MOM5-LR during MJJ. MOM5-LR-anom depicts a much stronger interannual SST variability than MOM5-LR during MJJ (Figure S7b). Overall, Figure S7 shows that the monthly climatology of the ATL3-averaged SST in MOM5-LR and MOM5-HR is well simulated even though it depicts a small warm bias. Monthly climatologies of the standard deviation of the ATL3-averaged SST anomalies from MOM5-LR and MOM5-HR have the correct phasing but the magnitude of the interannual SST variability is too weak throughout the year.

Next, the upper 200 m equatorial Atlantic temperature mean-state in ORA-S5, MOM5-LR and MOM5-HR is presented in Figures S8a, b, and c, respectively. Relative to ORA-S5 (Figure S8a), MOM5-LR (Figures S8b, d) has a too deep and diffusive thermocline. The simulation MOM5-LR depicts a 4 °C temperature bias at the thermocline level from 40°W to 0°E. Increasing the horizontal resolution from 1° for MOM5-LR to 0.25° for MOM5-HR leads to an improvement of the equatorial Atlantic Ocean temperature mean-state (Figures S8c, e). In particular, the thermocline is less diffusive and the ocean temperature bias is much reduced. Comparing the sensitivity experiment MOM5-LR-anom to MOM5-LR, we find that MOM5-LR-anom experiences a cooling ($\approx$ 0.4 °C) at the thermocline level but mainly between 40°W and 30°W and from 10°W to 10°E.

Furthermore, we compare the upper 200 m equatorial Atlantic Ocean interannual temperature variability in MJJ from MOM5-LR and MOM5-HR to ORA-S5 in Figure S9. Relative to ORA-S5 (Figure S9a), MOM5-LR depicts too weak interannual temperature variability in MJJ at the thermocline level along with a too deep thermocline (Figures S9b, d). In MOM5-HR, the ocean temperature variability bias in MJJ at the thermocline level is reduced but still present and the thermocline remains too deep (Figures S9c, e). Comparing MOM5-LR-anom to MOM5-LR (Figure S9f) shows that replacing JRA55-do wind anomalies for CORE-II wind anomalies leads to a strong increase of the upper 200 m interannual temperature variability in MJJ as discussed in the manuscript.

Finally, even though MOM5-LR and MOM5-HR feature some biases, such as a warm bias ($\approx$ 0.3 °C) in the ATL3 region and a too deep and diffusive thermocline, both simulations simulate reasonably well the tropical Atlantic mean-state as well as its monthly climatology and interannual SST and temperature variability, on a par with other OMIP2 models.

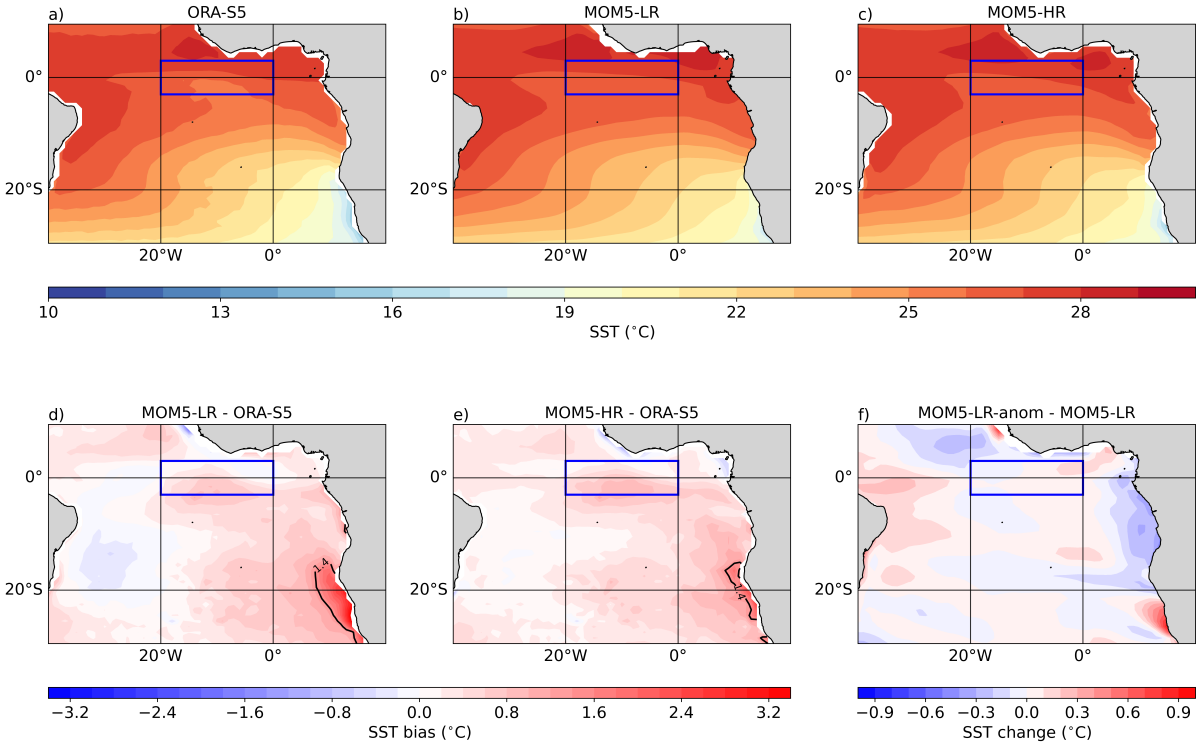

Figure S6. Tropical Atlantic mean SST over the period from January 1985 to December 2004 for (a) ORA-S5, (b) MOM5-LR, and (c) MOM5-HR. (d, e) Tropical Atlantic SST bias for MOM5-LR and MOM5-HR relative to ORA-S5, respectively. (f) Tropical Atlantic SST change MOM5-LR-anom relative to MOM5-LR. Note that panels (d, e) and (f) have different colorbar ranges.

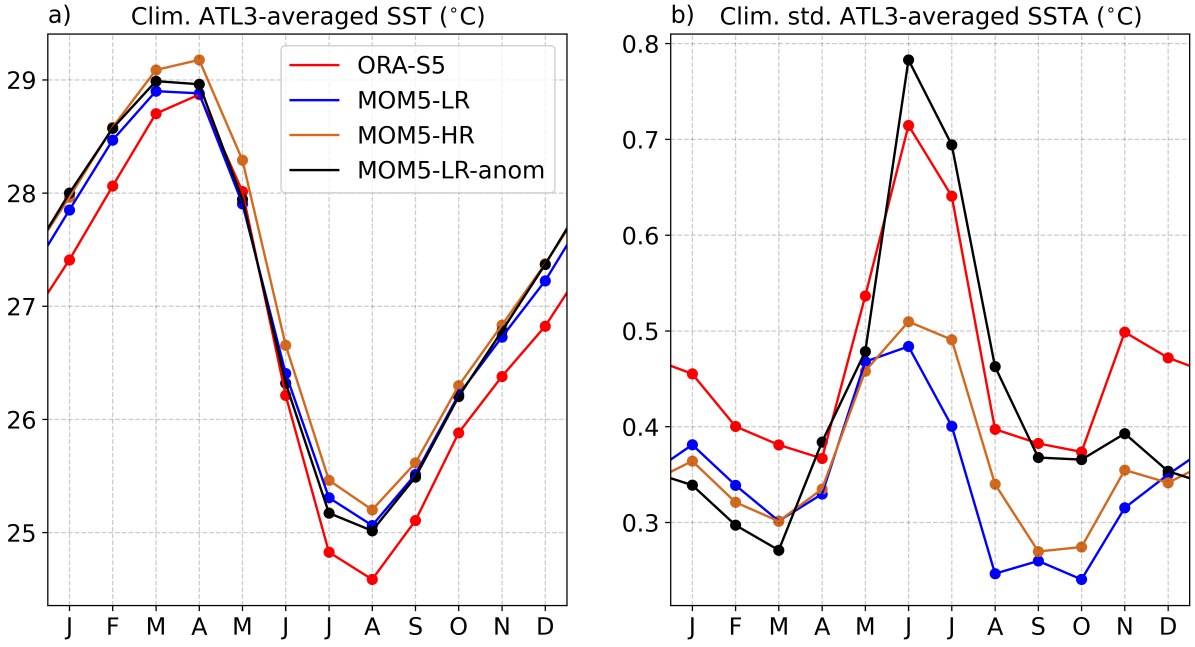

Figure S7. Monthly climatologies of (a) ATL3-averaged SSTs and (b) standard deviation of ATL3-averaged SST anomalies over the period from January 1985 to December 2004. Different colored lines corresponds to: (red) ORA-S5, (blue) MOM5-LR, (brown) MOM5-HR, and (black) MOM5-LR-anom.

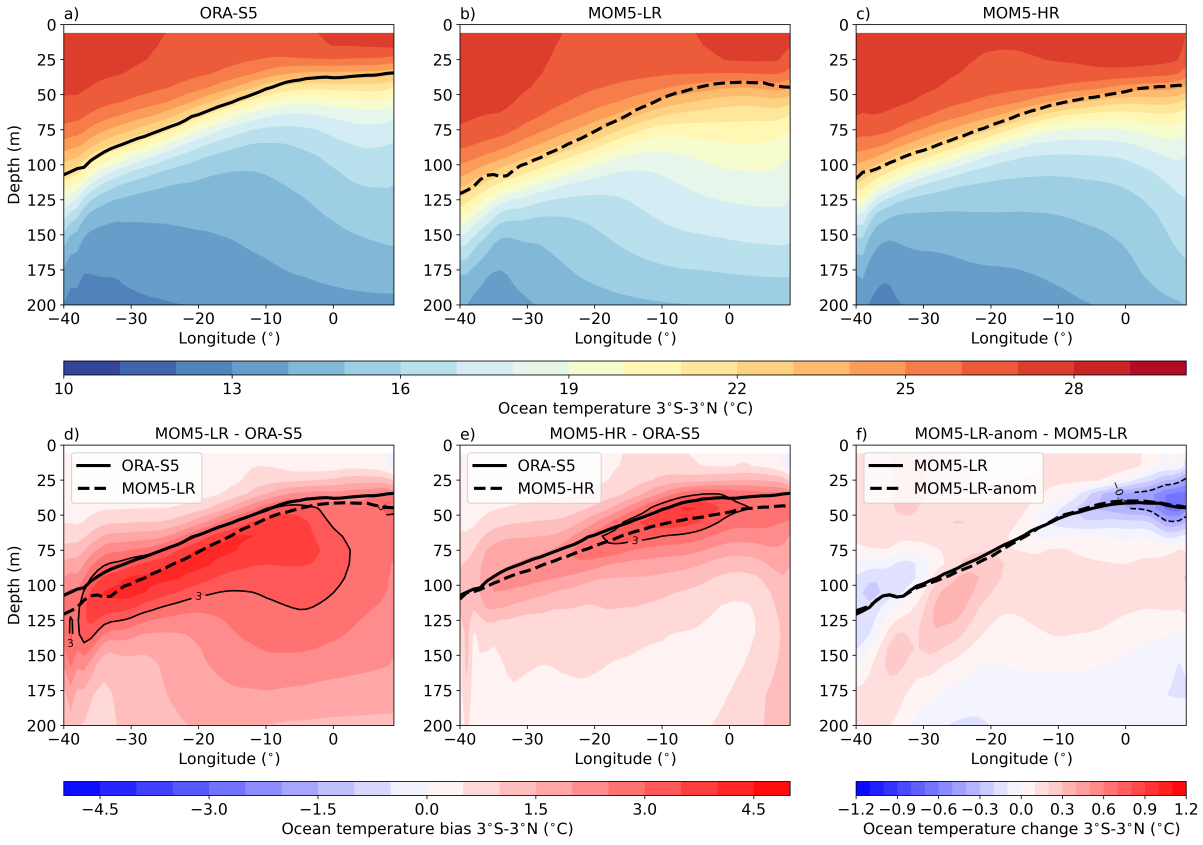

Figure S8. Same as Figure S6 but for the upper 200 m equatorial Atlantic Ocean temperature averaged between 3°S and 3°N.

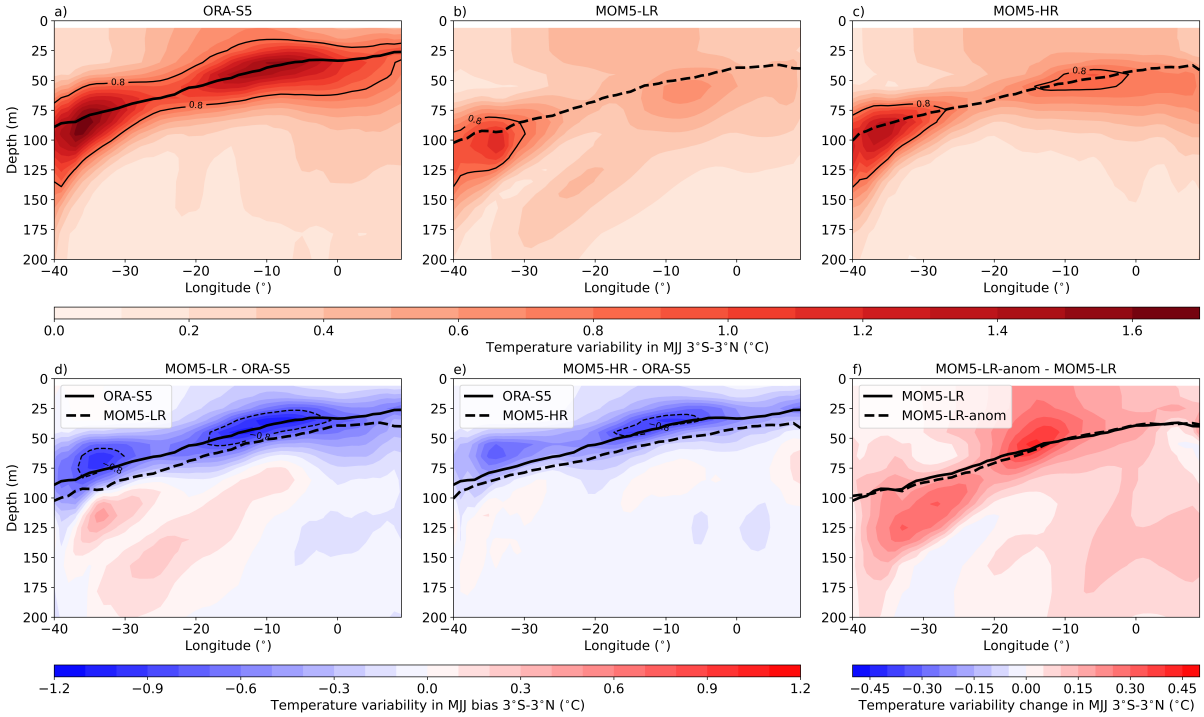

Figure S9. Same as Figure S6 but for the upper 200 m equatorial Atlantic Ocean temperature variability averaged between 3°S and 3°N in MJJ.

Supplementary Text S2: Assessment of OMIP1 and OMIP2 models against PIRATA data

In the following we compare the equatorial Atlantic (1°S-1°N) monthly climatologies of U10, SLA and SST from ORA-S5, OMIP1, and OMIP2 ensembles to the ones of the zonal wind at 4 m height, dynamic height and SST from the Prediction and Research Moored Array in the Tropical Atlantic (PIRATA; Servain et al., 1998; Bourlès et al., 2008) at 35°W, 23°W, 10°W, and 0°E.

Figures S10a-c show that the monthly climatology of zonal winds from CCMP-V2, CORE-II, and JRA55-do in the equatorial Atlantic align closely with PIRATA data in terms of phasing. Figure S10d indicates that the zonal wind recorded at the 35°W, 0°N PIRATA mooring is generally weaker compared to the reanalysis products throughout the year. However, it is worth mentioning that PIRATA wind measurements are taken at 4 m height, while the reanalysis products deliver data at 10 m height.

Figures S10e-h show that, compared to PIRATA data, the OMIP1 and OMIP2 ensembles accurately capture both the phasing and amplitude of the monthly climatology of SLA in the equatorial Atlantic. Similarly, Figures S10i-k illustrate that the phasing and amplitude of the monthly climatology of SST in the equatorial Atlantic are well represented by ORA-S5, OMIP1, and OMIP2 ensemble means. Finally, Figure S10l shows that the monthly climatology of SST from OMIP1 and OMIP2 at 10°W, 0°N closely resembles that from the PIRATA mooring at 10°W, albeit with a warm bias.

We can conclude that, despite the paucity of observed data available over the period from January 1985 to December 2004, both OMIP1 and OMIP2 ensemble means compare well with PIRATA.

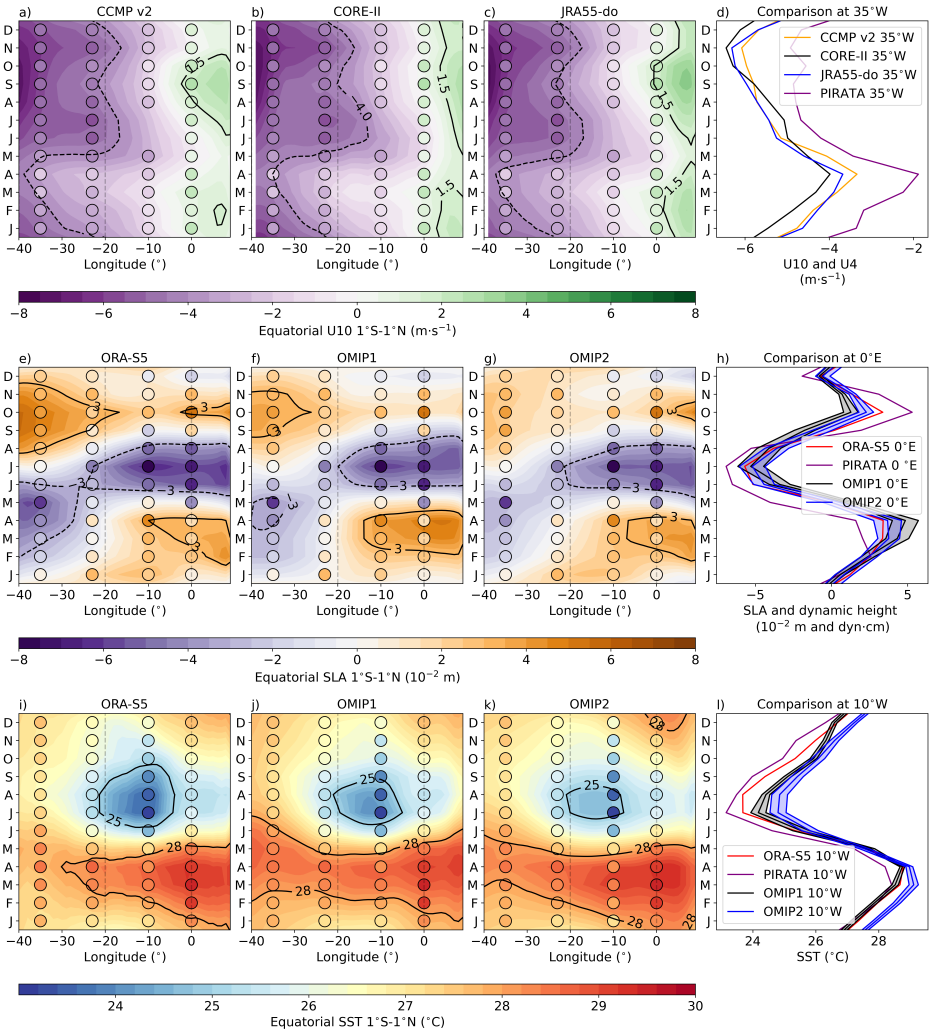

Figure S10. Hovmöller diagrams of monthly climatologies for equatorial Atlantic U10, SLA, and SST. (a) Monthly climatology of CCMP v2 U10, averaged between 1°S and 1°N, presented as a function of longitude and calendar month for the period January 1988 to December 2004. (b, c) Same as (a), but for CORE-II and JRA55-do U10 over the period January 1985 to December 2004. In (a, b, c) monthly climatologies derived using equatorial PIRATA mooring data at 35°W, 23°W, 10°W, and 0°E over the period from January 1985 to December 2004 are shown by colored dots. (d) Monthly climatologies of the zonal wind at 35°W, 0°N and at 10m height from CCMP v2 (orange), CORE-II (black), and JRA55-do (blue) and measured at 4 m height from the 35°W PIRATA mooring (purple). (e, f, g) Monthly climatologies of SLA in ORA-S5, OMIP1 ensemble mean, and OMIP2 ensemble mean, averaged between 1°S and 1°N, shown as a function of the longitude and calendar month for the period from January 1985 to December 2004. In (e, f, g) monthly climatologies of dynamic height derived using equatorial PIRATA mooring data at 35°W, 23°W, 10°W, and 0°E over the period from January 1985 to December 2004 are shown by colored dots. (h) Monthly climatologies of the SLA at 0°E, 0°N from ORA-S5 (red), OMIP1 (black), OMIP2 (blue) and dynamic height from the 0°E PIRATA mooring (purple). (i, j, k) Same as (e, f, g) but for the SST. (l) Monthly climatologies of SST at 10°W, 0°N from ORA-S5 (red), OMIP1 (black), OMIP2 (blue) and from the 10°W PIRATA mooring (purple).

Supplementary Text S3: Fidelity of different wind reanalyses

In Figure S11, we compare different wind reanalysis products over the period from January 1985 to December 2004. The considered reanalyses are: the NCEP/NCAR Reanalysis 1 (NCEP-R1; Kalnay et al., 1996), which is available at a horizontal resolution of 2.5° by 2.5° and covers the period from January 1948 to present day; the NCEP/DOE Reanalysis 2 (NCEP/DOE-R2; Kanamitsu et al., 2002), which is available at a horizontal resolution of 2.5° by 2.5° from January 1979 to present day; the fifth generation of the European Centre for Medium-Range Weather Forecast (ECMWF) reanalysis (ERA5; Hersbach et al., 2023), with a horizontal resolution of 0.25° by 0.25°, spanning the period January 1940 to present day; the CORE-II forcing (Large and Yeager, 2009), with a horizontal resolution of 2° by 2° and a temporal resolution of 6 hours encompassing the period from January 1948 to December 2009; and finally the JRA55-do forcing derived from the Japanese 55 years Reanalysis (Griffies et al., 2016; Tsujino et al., 2018), with a horizontal resolution of 0.5625° × 0.5625° (∼ 55 km × 55 km at the equator) and a temporal resolution of 3 hours spanning from January 1958 to December 2022.

All of these reanalysis products depict a similar monthly climatology of the ATL4-averaged zonal winds, characterised by the weakest zonal winds in March and April, followed by a strengthening of the easterly winds from May to November (Figure S11a). Notably, NCEP-R1 displays consistently weaker easterlies throughout the year (Figure S11a). Taking the CCMP v2 climatology as a reference, the root mean square error of the monthly climatology is 0.39 $m{\cdot}s^{-1}$ for CORE-II and is 0.27 $m{\cdot}s^{-1}$ for JRA55-do. When examining zonal wind variability in the western equatorial Atlantic, the amplitude of zonal wind variability between CORE-II and JRA55-do is relatively similar, but JRA55-do reaches its peak in April, while CORE-II's peak occurs in May (Figure S11b).

The examination of extended timeseries of zonal wind anomalies in the ATL4 region for both the JRA55-do (over the period 1958 to 2022) and the CORE-II (over the period 1948 to 2007), shows that both forcing datasets have their maximum variability in May (Figure S12). This highlights that the disparity in the timing of the peak of the zonal wind variability between JRA55-do and CORE-II (Figure S11b) within the ATL4 region is linked to the specific time periods under consideration. ERA5 depicts the largest zonal wind variability and peaks in April (Figure S11b). Both NCEP/DOE-R2 and NCEP-R1 exhibit the smallest zonal wind variability, with both reaching their peaks in May (Figure S11b). Taking the CCMP v2 monthly climatological standard deviation of the ATL4-averaged zonal wind anomalies as a reference, the root-mean-square error for CORE-II is 0.15 $m{\cdot}s^{-1}$ and it is 0.09 $m{\cdot}s^{-1}$ for JRA55-do. The correlation matrix, spanning January 1988 to December 2004, shows the Pearson correlation coefficients between the ATL4-averaged zonal wind anomalies from the different reanalysis products (Figure S13). Specifically, it shows that the Pearson correlation coefficient between CCMP v2 and CORE-II is 0.81, while it is 0.89 for JRA55-do (Figure S13). In addition, the Pearson correlation coefficients for ERA5 in relation to CORE-II and JRA55-do are 0.82 and 0.90, respectively (Figure S13).

Additionally, we note that JRA55-do, ERA5 and NCEP/DOE-R2 have a secondary peak in February (Figure S11b), whereas this secondary peak is notably weaker in CORE-II and NCEP-R1. In comparison to the CORE-II forcing, the peak of zonal wind variability during February found in the JRA55-do forcing results from a few strong events occurring between 1985 and 2004 (Figure S14a). Figures S14b-c depict zonal wind anomalies in the western equatorial Atlantic for April and May, respectively. These figures highlight that zonal winds anomalies in April are more pronounced in JRA55-do compared to CORE-II, while the reverse is observed in May.

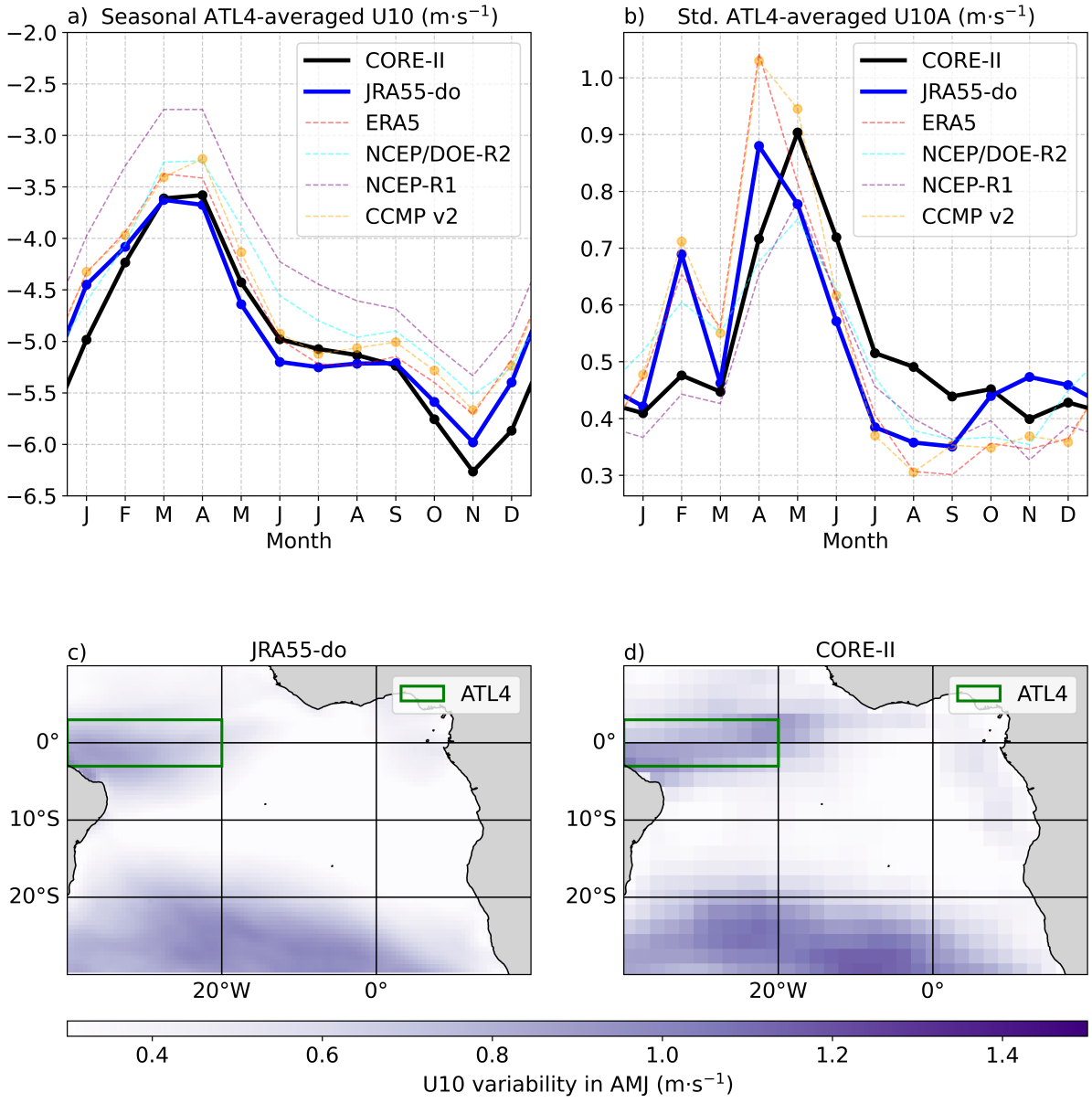

Figure S11. Western equatorial Atlantic U10 monthly climatologies for the period from January 1985 to December 2004. (a) ATL4-averaged monthly climatologies of U10 winds. (b) Monthly climatologies of the standard deviation of U10 anomalies averaged over the ATL4 region. Different lines correspond to various reanalysis products: (black) CORE-II, (blue) JRA55-do, (red) ERA5, (cyan) NCEP/DOE-R2, (purple) NCEP-R1, and (orange) CCMP v2. (c, d) Standard deviation of U10 anomalies over the tropical Atlantic during AMJ for JRA55-do and CORE-II, respectively.

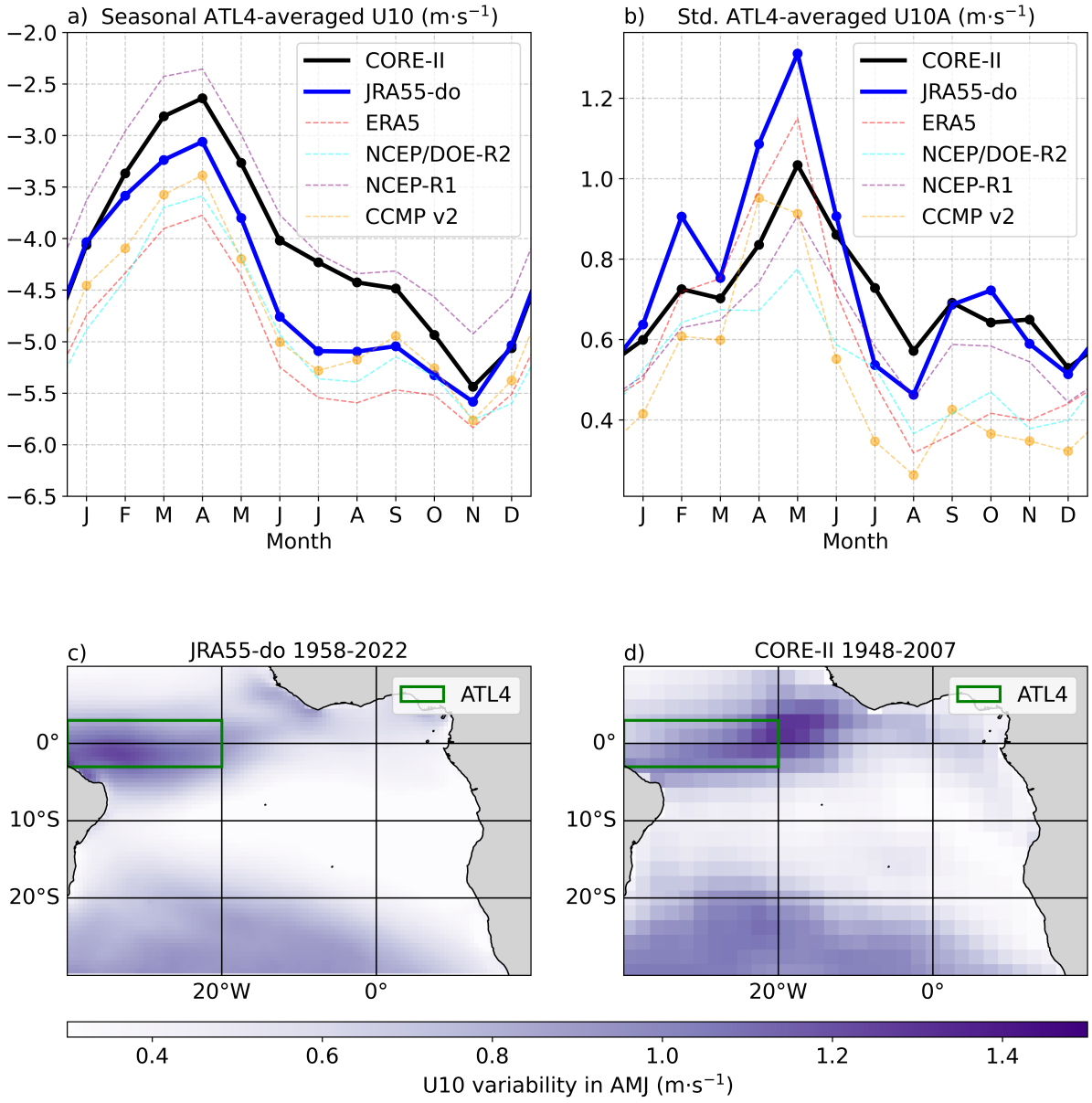

Figure S12. Same as Figure S11 but for extended time periods. CORE-II is taken from January 1948 to December 2007, JRA55-do from January 1958 to December 2022, ERA5 from January 1940 to December 2022, NCEP/DOE-R2 from January 1979 to December 2022, NCEP-R1 from January 1948 to December 2022, and CCMP v2 from January 1988 to December 2017.

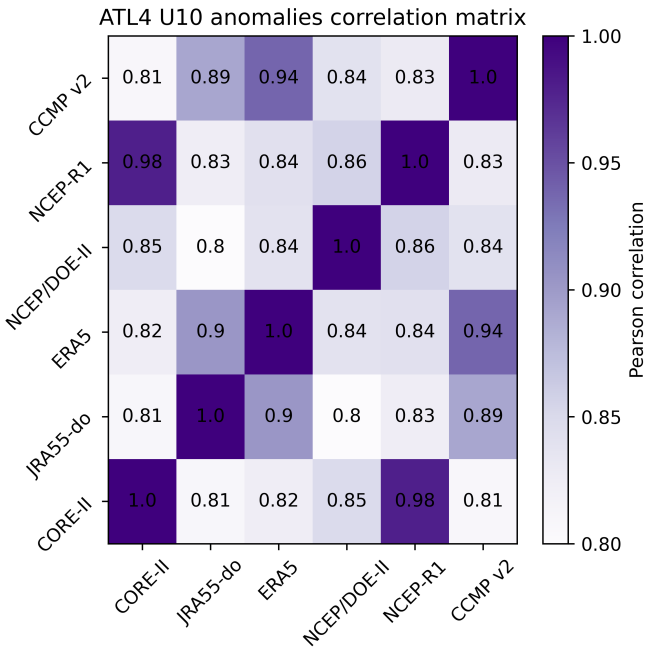

Figure S13. Correlation matrix for zonal wind anomalies at 10 m height in the western equatorial Atlantic. Correlation coefficients are based on Pearson correlation coefficients evaluated over the period January 1988 to December 2004. The datasets included in the matrix are: CCMP v2, NCEP-R1, NCEP/DOE-II, ERA5, JRA55-do, and CORE-II.

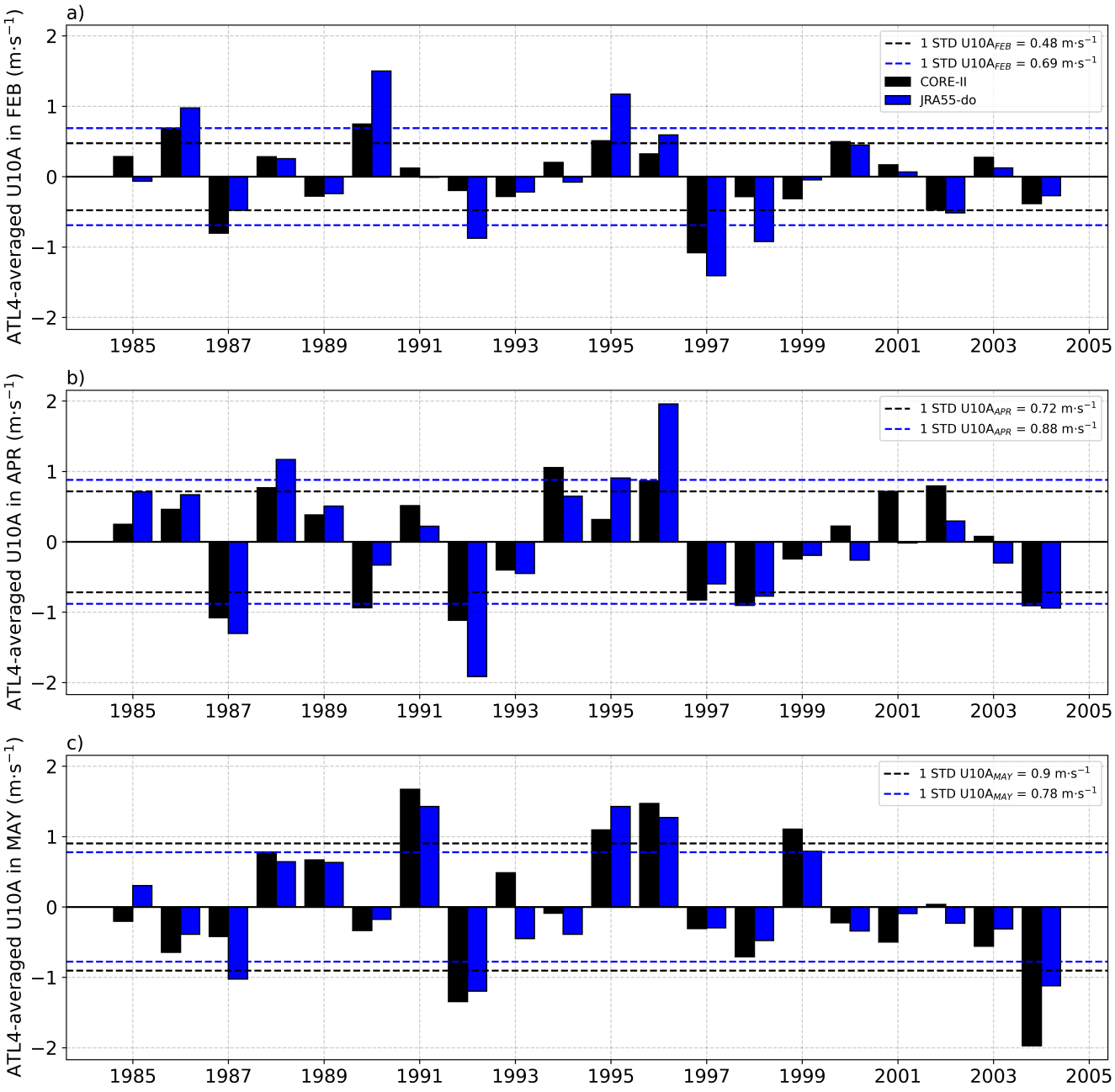

Figure S14. Western equatorial Atlantic zonal wind anomalies at 10 m height. (a) Timeseries of the ATL4-averaged February U10 anomalies spanning the period from January 1985 to December 2004, using CORE-II (black) and JRA55-do (blue) reanalysis products. (b) Same as (a) but for April. (c) Same as (a) but for May. Black (Blue) dashed lines represent $\pm$ 1 standard deviation of the U10 anomalies.

Model Name	Ocean Model	Ocean Grid Points (nlon × nlat × nlevel)	Atmospheric Model	Atmospheric Grid Points (nlon × nlat × nlevel)
ACCESS-CM2	MOM5	360 × 300 × 50	MetUM-HadGEM3-GA7.1	192 × 144 × 85
ACCESS-ESM1-5	MOM5	360 × 300 × 50	HadGAM2	192 × 145 × 38
BCC-CSM2-MR	MOM4	360 × 232 × 40	BCC-AGCM3-MR	320 × 160 × 46
BCC-ESM1	MOM4	360 × 232 × 40	BCC-AGCM3-LR	128 × 64 × 26
CAMS-CSM1-0	MOM4	360 × 200 × 50	ECHAM5-CAMS	320 × 160 × 31
CAS-ESM2-0	LICOM2.0	362 × 196 × 30	IAP AGCM 5.0	256 × 128 × 35
CESM2	POP2	320 × 384 × 60	CAM6	288 × 192 × 32
CESM2-FV2	POP2	320 × 384 × 60	CAM6	144 × 96 × 32
CESM2-WACCM	POP2	320 × 384 × 60	WACCM6	288 × 192 × 70
CESM2-WACCM-FV2	POP2	320 × 384 × 60	WACCM6	144 × 96 × 70
CIESM	CIESM-OM	720 × 560 × 46	CIESM-AM	288 × 192 × 30
CMCC-CM2-HR4	NEMO3.6	1442 × 1051 × 50	CAM4	288 × 192 × 26
CMCC-CM2-SR5	NEMO3.6	362 × 292 × 50	CAM5.3	288 × 192 × 30
CMCC-ESM2	NEMO3.6	362 × 192 × 50	CAM5.3	288 × 192 × 30
CanESM5	NEMO3.4.1	361 × 290 × 45	CanAM5	128 × 64 × 49
CanESM5-1	NEMO3.4.1	360 × 290 × 45	CanAM5.1	128 × 64 × 49
E3SM-1-0	MPAS-O	320 × 384 × 75	EAM1.0	90 × 90 × 72
E3SM-1-1	MPAS-O	320 × 384 × 75	E3SMv1.1	90 × 90 × 72
E3SM-1-1-ECA	MPAS-O	320 × 384 × 75	E3SMv1.1	90 × 90 × 72
EC-Earth3	NEMO3.6	362 × 292 × 75	IFS cy36r4	512 × 256 × 91
EC-Earth3-AerChem	NEMO3.6	362 × 292 × 75	IFS cy36r4	512 × 256 × 91
EC-Earth3-CC	NEMO3.6	362 × 292 × 75	IFS cy36r4	512 × 256 × 91
EC-Earth3-Veg	NEMO3.6	362 × 292 × 75	IFS cy36r4	512 × 256 × 91
EC-Earth3-Veg-LR	NEMO3.6	362 × 292 × 75	IFS cy36r4	320 × 160 × 62
FGOALS-f3-L	LICOM3.0	360 × 218 × 30	FAMIL2.2	360 × 180 × 32
FIO-ESM-2-0	POP2-W	320 × 384 × 60	CAM4	192 × 288 × 26
GFDL-CM4	GFDL-OM4p25	1440 × 1080 × 75	GFDL-AM4.0.1	360 × 180 × 33
GFDL-ESM4	GFDL-OM4p5	720 × 576 × 75	GFDL-AM4.1	360 × 180 × 49
GISS-E2-1-G	GISS Ocean GO1	360 × 180 × 40	GISS-E2.1	144 × 90 × 40

Table S1. Table summarising the CMIP6 model simulations used in Figure 1.

Model Name	Ocean Model	Ocean Grid Points (nlon × nlat × nlevel)	Atmospheric Model	Atmospheric Grid Points (nlon × nlat × nlevel)
GISS-E2-1-G-CC	GISS Ocean GO1	360 × 180 × 40	GISS-E2.1	144 × 90 × 40
GISS-E2-1-H	HYCOM Ocean	360 × 180 × 32	GISS-E2.1	144 × 90 × 40
GISS-E2-2-G	GISS Ocean GO1	360 × 180 × 40	GISS-E2.2	144 × 90 ×102
GISS-E2-2-H	HYCOM Ocean	360 × 180 × 32	GISS-E2.2	144 × 90 × 102
GISS-E3-G	GISS Ocean GO1	360 × 180 × 32	GISS-E3	90 × 90 × 102
IITM-ESM	MOM4p1	360 × 200 × 50	IITM-GFSv1	192 × 94 × 64
INM-CM4-8	INM-OM5	360 × 318 × 40	INM-AM4-8	180 × 120 × 21
INM-CM5-0	INM-OM5	720 × 720 × 40	INM-AM5-0	180 × 120 × 73
IPSL-CM5A2-INCA	NEMO-OPA3.6	182 × 149 × 31	LMDZ-APv5	96 × 96 × 39
IPSL-CM6A-LR	NEMO-OPA eORCA1.3	362 × 332 × 75	LMDZ-NPv6	144 × 143 × 79
PSL-CM6A-LR-INCA	NEMO-OPA eORCA1.3	362 × 332 × 75	LMDZ-NPv6	144 × 143 × 79
KACE-1-0-G	MOM4p1	360 × 200 × 50	MetUM-HadGEM3-GA7.1	192 × 144 × 85
KIOST-ESM	GFDL-MOM5	360 × 200 × 52	GFDL-AM2.0	192 × 96 × 32
MCM-UA-1-0	MOM1	192 × 80 × 18	MCMv1	96 × 80 × 14
MIROC6	COCO4.9	360 × 256 × 63	CCSR-AGCM	256 × 128 × 81
MPI-ESM-1-2-HAM	MPIOM1.6	256 × 220 × 40	ECHAM6.3	192 × 96 × 47
MPI-ESM1-2-HR	MPIOM1.6	802 × 404 × 40	ECHAM6.3	384 × 192 × 95
MPI-ESM1-2-LR	MPIOM1.6	256 × 220 × 40	ECHAM6.3	192 × 96 × 47
MRI-ESM2-0	MRI.COM4.4	360 × 364 × 61	MRI-AGCM3.5	320 × 160 × 80
NESM3	NEMO3.4	384 × 362 × 46	ECHAM6.3	192 × 96 × 47
NorCPM1	MICOM1.1	320 × 384 × 53	CAM-OSLO4.1	144 × 96 × 26
NorESM2-LM	MICOM	360 × 384 × 70	CAM-OSLO	144 × 96 × 32
NorESM2-MM	MICOM	1440 × 1152 × 70	CAM-OSLO	288 × 192 × 32
SAM0-UNICON	POP (2)	320 × 384 × 60	CAM5.3-UNICON	288 × 192 × 30
TaiESM1	POP (2)	320 × 384 × 60	TaiAM1	288 × 192 × 30

Table S1. Table summarising the CMIP6 model simulations used in Figure 1 (continued).

Data availability.

The ORA-S5 data is publicly available at the link: https://cds.climate.copernicus.eu/cdsapp#!/dataset/reanalysis-oras5?tab=form. The OI-SST data is publicly available at the link: https://psl.noaa.gov/data/gridded/data.noaa.oisst.v2.html. The CCMP v2 data is publicly available at the following link: https://apdrc.soest.hawaii.edu/erddap/griddap/hawaii_soest_3387_f2e3_e359.html. The AVISO SLA was retrieved at the following link: https://cds.climate.copernicus.eu/cdsapp#!/dataset/10.24381/cds.4c328c78?tab=overview. The NCEP-R1 data is publicly available at the following link: https://psl.noaa.gov/data/gridded/data.ncep.reanalysis.html. The NCEP/DOE-R2 data is publicly available at the following link: https://psl.noaa.gov/data/gridded/data.ncep.reanalysis2.html. The ERA5 data is available at the following link: https://cds.climate.copernicus.eu/cdsapp#!/dataset/reanalysis-era5-single-levels-monthly-means?tab=form. The OMIP1 and OMIP2 model output data were downloaded at the following link: https://esgf-data.dkrz.de/projects/esgf-dkrz/. The CORE-II forcing is available at the following link: https://data1.gfdl.noaa.gov/nomads/forms/core/COREv2.html. The JRA55-do forcing is available at the following link: https://climate.mri-jma.go.jp/pub/ocean/JRA55-do/. The PIRATA data can be downloaded at the following link: https://www.pmel.noaa.gov/gtmba/pmel-theme/atlantic-ocean-pirata. The MOM5-LR, MOM5-LR-anom, and MOM5-HR datasets used in this study can be retrieved from Farneti (2024).

References

Bourlès, B., Lumpkin, R., McPhaden, M. J., Hernandez, F., Nobre, P., Campos, E., Yu, L., Planton, S., Busalacchi, A., Moura, A. D., Servain, J., and Trotte, J.: THE PIRATA PROGRAM: History, Accomplishments, and Future Directions*, Bulletin of the American Meteorological Society, 89, 1111 – 1126, https://doi.org/10.1175/2008BAMS2462.1, 2008.

Farneti, R.: Output files for MOM5 driven by JRA55-do at 1-degree and 0.25-degree horizontal resolution, https://doi.org/10.5281/zenodo.11047949, 2024.

Farneti, R., Stiz, A., and Ssebandeke, J. B.: Improvements and persistent biases in the southeast tropical Atlantic in CMIP models, npj Climate and Atmospheric Science, 5, 42, https://doi.org/10.1038/s41612-022-00264-4, 2022.

Griffies, S. M., Danabasoglu, G., Durack, P. J., Adcroft, A. J., Balaji, V., Böning, C. W., Chassignet, E. P., Curchitser, E., Deshayes, J., Drange, H., Fox-Kemper, B., Gleckler, P. J., Gregory, J. M., Haak, H., Hallberg, R. W., Heimbach, P., Hewitt, H. T., Holland, D. M., Ilyina, T., Jungclaus, J. H., Komuro, Y., Krasting, J. P., Large, W. G., Marsland, S. J., Masina, S., McDougall, T. J., Nurser, A. J. G., Orr, J. C., Pirani, A., Qiao, F., Stouffer, R. J., Taylor, K. E., Treguier, A. M., Tsujino, H., Uotila, P., Valdivieso, M., Wang, Q., Winton, M., and Yeager, S. G.: OMIP contribution to CMIP6: experimental and diagnostic protocol for the physical component of the Ocean Model Intercomparison Project, Geoscientific Model Development, 9, 3231–3296, https://doi.org/10.5194/gmd-9-3231-2016, 2016.

Hersbach, H., Bell, B., Berrisford, P., Biavati, G., Horányi, A., Muñoz Sabater, J., Nicolas, J., Peubey, C., Radu, R., Rozum, I., Schepers, D., Simmons, A., Soci, C., Dee, D., and Thépaut, J.-N.: ERA5 monthly averaged data on single levels from 1940 to present, Copernicus Climate Change Service (C3S) Climate Data Store (CDS), 2023.

Kalnay, E., Kanamitsu, M., Kistler, R., Collins, W., Deaven, D., Gandin, L., Iredell, M., Saha, S., White, G., Woollen, J., Zhu, Y., Chelliah, M., Ebisuzaki, W., Higgins, W., Janowiak, J., Mo, K. C., Ropelewski, C., Wang, J., Leetmaa, A., Reynolds, R., Jenne, R., and Joseph, D.: The NCEP/NCAR 40-Year Reanalysis Project, Bulletin of the American Meteorological Society, 77, 437 – 472, https://doi.org/https://doi.org/10.1175/1520-0477(1996)077<0437:TNYRP>2.0.CO;2, 1996.

Kanamitsu, M., Ebisuzaki, W., Woollen, J., Yang, S.-K., Hnilo, J. J., Fiorino, M., and Potter, G. L.: NCEP–DOE AMIP-II Reanalysis (R-2), Bulletin of the American Meteorological Society, 83, 1631 – 1644, https://doi.org/https://doi.org/10.1175/BAMS-83-11-1631, 2002.

Large, W. G. and Yeager, S. G.: The global climatology of an interannually varying air–sea flux data set, Climate Dynamics, 33, 341–364, https://doi.org/10.1007/s00382-008-0441-3, 2009.

Servain, J., Busalacchi, A. J., McPhaden, M. J., Moura, A. D., Reverdin, G., Vianna, M., and Zebiak, S. E.: A Pilot Research Moored Array in the Tropical Atlantic (PIRATA), Bulletin of the American Meteorological Society, 79, 2019 – 2032, https://doi.org/10.1175/1520-0477(1998)079<2019:APRMAI>2.0.CO;2, 1998.

Tsujino, H., Urakawa, S., Nakano, H., Small, R. J., Kim, W. M., Yeager, S. G., Danabasoglu, G., Suzuki, T., Bamber, J. L., Bentsen, M., Böning, C. W., Bozec, A., Chassignet, E. P., Curchitser, E., Boeira Dias, F., Durack, P. J., Griffies, S. M., Harada, Y., Ilicak, M., Josey, S. A., Kobayashi, C., Kobayashi, S., Komuro, Y., Large, W. G., Le Sommer, J., Marsland, S. J., Masina, S., Scheinert, M., Tomita, H., Valdivieso, M., and Yamazaki, D.: JRA-55 based surface dataset for driving ocean–sea-ice models (JRA55-do), Ocean Modelling, 130, 79–139, https://doi.org/https://doi.org/10.1016/j.ocemod.2018.07.002, 2018.